Reduction Mechanism for CeO_2 Revealed by Direct Observation of the Oxygen Vacancy Distribution in Shape-Controlled CeO_2

Hojo, Hajime
Faculty of Engineering Sciences, Kyushu University

Hirota, Kazuki
Graduate School of Engineering Sciences, Kyushu University

Ito, So
Graduate School of Engineering Sciences, Kyushu University

Einaga, Hisahiro
Faculty of Engineering Sciences, Kyushu University

出版情報：Advanced Materials Interfaces. 10 (6), pp.2201954-, 2023-02-23. Wiley
バージョン：

ADVANCED MATERIALS INTERFACES
www.advmatinterfaces.de

Reduction Mechanism for CeO_2 Revealed by Direct Observation of the Oxygen Vacancy Distribution in Shape-Controlled CeO_2

Hajime Hojo, Kazuki Hirota, So Ito, and Hisahiro Einaga*

CeO_2 and CeO_2-based materials are widely used as catalysts and catalyst supports for a variety of chemical reactions. The ability to form oxygen vacancies plays an important role in the catalytic activities in these materials. Therefore, revealing the reduction mechanism for CeO_2 is crucial to understanding the catalytic activities. In this study, shape-controlled CeO_2 nanoparticles are fabricated and the distribution of surface oxygen vacancies on the (100) and (111) surfaces is systematically studied using scanning transmission electron microscopy and electron energy-loss spectroscopy and the response to H_2 reduction treatment. It is successfully demonstrated that both catalytic activities and the ability to form oxygen vacancies are strongly dependent on the type of lattice planes. Moreover, the present results provide important insights into the reduction mechanism for CeO_2, in which bulk oxygen instead of the widely believed surface capping oxygen makes no small contribution to the initial reduction step.

1. Introduction

CeO_2 and CeO_2-containing materials have attracted much attention as catalysts and supports for supported metal catalysts for various catalytic reactions,[1,2] which often utilize the ability of CeO_2 to easily release and store oxygen via the formation of oxygen vacancies. Therefore, revealing the reduction mechanism is crucial to understanding the catalytic activities. Temperature-programmed reduction (TPR) measurements using H_2 as a reducing agent (H_2-TPR) are widely performed to study the reactivity of lattice oxygen, and, hence, the reduction process for CeO_2 and CeO_2-based materials.[3–7] It is well known that the H_2-TPR profile for CeO_2 primarily has two peaks. Based on the H_2-TPR data obtained for CeO_2 with different specific surface areas, the low-temperature peak below 600 °C is attributed to the reduction of the "surface capping oxygen" or "surface oxygen", while the high-temperature signal observed above 600 °C is attributed to removal of "bulk oxygen".[8] Although this interpretation has been widely accepted, studies that directly relate the H_2-profiles and the distribution of oxygen vacancies for CeO_2 have not been reported.

On the other hand, nanostructured CeO_2-based materials have attracted much attention due to their peculiar properties,[9–11] and several studies have reported using shape-controlled nanoparticles and nanorods for CeO_2 that the (100) and (110) planes are more reactive than the (111) planes.[4,12,13] Such a different behavior is generally explained based on the results of theoretical calculations that show that the formation energies of oxygen vacancies are smaller for the (100) and/or (110) planes than for the (111) plane.[14–18] Therefore, the reduction process for CeO_2 can also be different depending on the crystal planes. Experimentally, it has been reported that (100) planes are more easily reduced than (111) planes based on UV Raman spectroscopy[19] and H_2-TPR measurements.[20] However, information for the distribution of oxygen vacancies is lacking. A recent advantage in scanning transmission electron microscopy (STEM) has enabled us to study the valence state of metal oxides at the atomic scale using electron energy loss spectroscopy (EELS). STEM-EELS has been applied to CeO_2 to study the distribution of Ce^{3+}, and, hence, the oxygen vacancies, at the grain boundaries[21–23] and surfaces.[24–27] Although it was suggested that fewer oxygen vacancies are present on the (111) planes than on the (100) planes,[25,27] there has been no report that has systemically studied the amount/distribution of oxygen vacancies and their response to reduction treatments.

In this study, to reveal the reduction mechanism for CeO_2, we synthesized CeO_2 nanoparticles with cubic and octahedral shapes, in which the (100) and (111) planes are mainly exposed, respectively, and investigated the distribution of oxygen vacancies in these nanoparticles using STEM-EELS and their response to reduction treatments. Together with the results of

H. Hojo, H. Einaga
Faculty of Engineering Sciences
Kyushu University
Fukuoka 816-8580, Japan
E-mail: hojo.hajime.100@m.kyushu-u.ac.jp
K. Hirota, S. Ito
Graduate School of Engineering Sciences
Kyushu University
Fukuoka 816-8580, Japan

The ORCID identification number(s) for the author(s) of this article can be found under https://doi.org/10.1002/admi.202201954.

DOI: 10.1002/admi.202201954

H_2-TPR measurements and the catalytic properties of these samples, the reduction mechanism for CeO_2 is discussed.

2. Results and Discussion

CeO_2 nanoparticles with cubic and octahedral shapes were prepared using a hydrothermal method (see details in the Experimental Section). **Figure 1**a,b shows typical high-angle annular dark-field (HAADF) images of cubic and octahedral nanoparticles synthesized in this study. The X-ray diffraction (XRD) patterns for these samples can be indexed to a pure cubic phase of CeO_2 (Figure S1, Supporting Information). Hereafter, we call these nanoparticles c-CeO_2 and o-CeO_2, respectively. The size of the c-CeO_2 and o-CeO_2 nanoparticles ranges from ≈20 to 80 nm and from ≈80 to 250 nm, respectively. It should be noted that the size of o-CeO_2 is defined as the cube root of the volume of the octahedral CeO_2 to enable easier comparison with the size of c-CeO_2. That is, the effective size of o-CeO_2, r_o, corresponds to $0.56 \times h_o$, where h_o is the length of the octahedral diagonal. Although some of the nanoparticles do not have well-defined shapes when the nanoparticles are small, especially for c-CeO_2, the degree of shape control turns out to be good enough to observe the crystal plane dependence of the activities of lattice oxygen, as will be discussed below. The Brunauer–Emmett–Teller (BET) specific surface areas for c-CeO_2 and o-CeO_2 are 7.6 and 4.2 $m^2\ g^{-1}$, respectively. The higher specific surface area of c-CeO_2 reflects the smaller size of c-CeO_2 compared to o-CeO_2.

To investigate the reactivity of lattice oxygen in c-CeO_2 and o-CeO_2, H_2-TPR measurements were performed. The TPR of CeO_2 primarily shows two peaks, as shown in Figure 1c. As discussed in the Introduction, it has been reported that the low-temperature peak below 600 °C corresponds to the reduction of the "surface oxygen" of CeO_2, while the high-temperature signal above 600 °C is attributed to the removal of "bulk oxygen".[8] Interestingly, the low-temperature peak of c-CeO_2 (≈330 °C) is centered at a much lower temperature than o-CeO_2 (≈520 °C), indicating that the reactivity of lattice oxygen is higher for the (100) planes than for the (111) planes. Compared to previous reports for H_2-TPR for shape-controlled CeO_2,[5,20] the low-temperature peaks and their systematic shifts are clearly visible, demonstrating the highly shape-controlled nature of the c-CeO_2 and o-CeO_2 used in this study. The amount of the "surface oxygen" that contributes to the first peak was estimated

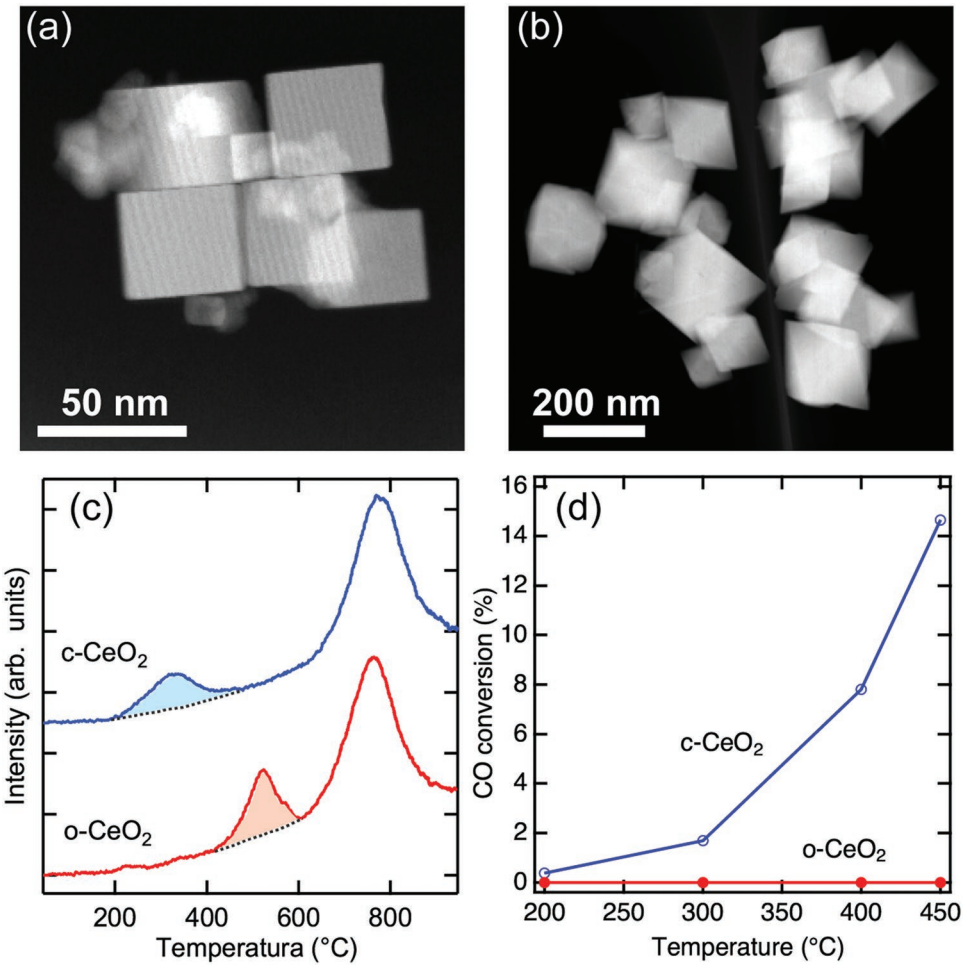

Figure 1. HAADF STEM images of CeO_2 nanoparticles with a) cubic (c-CeO_2) and b) octahedral (o-CeO_2) shapes. c) H_2-TPR profiles for c-CeO_2 and o-CeO_2. d) Catalytic CO oxidation over c-CeO_2 and o-CeO_2.

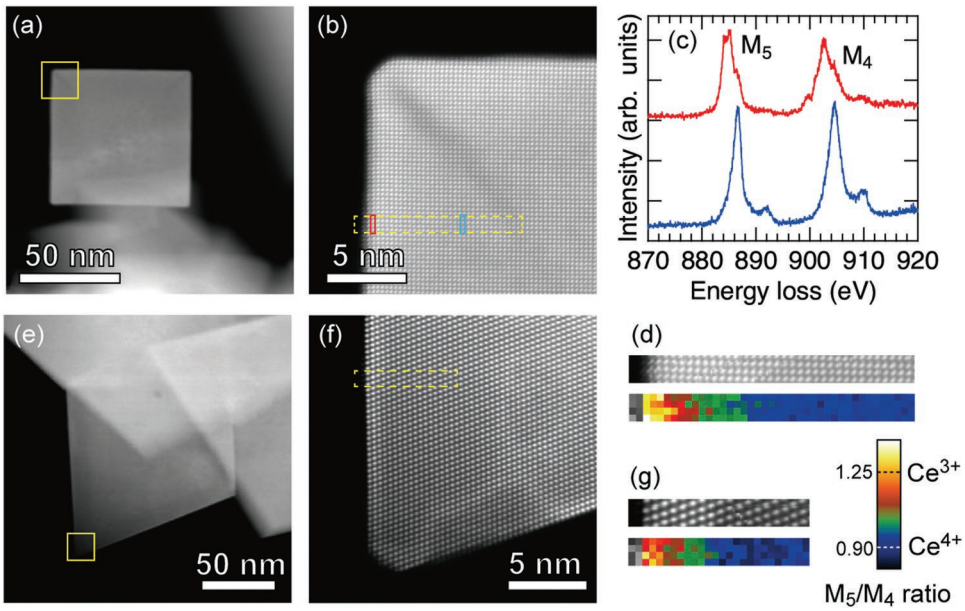

Figure 2. a) HAADF STEM image of c-CeO_2. b) Magnified HAADF image of the region marked with a yellow square in (a). c) Ce $M_{4,5}$-edge EELS spectra taken from the surface region and the interior region of the nanoparticle; each region is marked with red and blue rectangles in (b), respectively. d) M_5/M_4 ratio map and simultaneously obtained HAADF image taken from the region shown by the yellow-dotted rectangle in (b). e) HAADF STEM image of o-CeO_2. f) Magnified HAADF image at the region marked with a yellow square in (e). g) M_5/M_4 ratio map and simultaneously obtained HAADF image taken from the region shown by the yellow-dotted rectangle in (f).

from the filled area in Figure 1c to have a c-CeO_2 to o-CeO_2 ratio of 0.76:1. This result indicates that c-CeO_2 contains less lattice oxygen that can react below ≈600 °C compared to o-CeO_2. We will discuss the origin of the first peak after introducing the STEM-EELS results. Figure 1d compares the temperature dependence of CO oxidation activity for c-CeO_2 and o-CeO_2. c-CeO_2 shows higher CO oxidation activity than o-CeO_2. It was reported that CO oxidation over CeO_2 proceeds via the so-called Mars-van Krevelen mechanism, in which the lattice oxygen of CeO_2 is used for the reaction.[1,12] Therefore, this result also demonstrates that lattice oxygen is more active for the (100) planes.

To reveal the local distribution of oxygen vacancies at the surface of c-CeO_2 and o-CeO_2, STEM-EELS measurements were conducted with the nanoparticles oriented along the [001] and [011] zone axes, respectively. **Figure 2**a shows a typical HAADF image of a cubic CeO_2 nanoparticle with a size of ≈70 nm. The magnified HAADF image shown in Figure 2b clearly demonstrates that the (100) planes are mainly exposed. Figure 2c shows the Ce $M_{4,5}$-edge EELS spectra taken at the surface region and the interior region of the nanoparticle. It is known that the M_5/M_4 intensity ratio is related to the valence state of Ce, and the M_5/M_4 ratio is ≈0.90 and 1.25 for Ce^{4+} and Ce^{3+}, respectively.[21] To quantitatively determine the valence state of Ce, the M_5/M_4 intensity ratios were calculated using the positive part of the second derivative of the experimental spectra. As expected from the nominal valence state of Ce in CeO_2, the M_5/M_4 ratio in the interior region was determined to be 0.90. On the other hand, the M_5/M_4 ratio at the surface region was 1.27. This result suggests that the valence state of Ce is close to 3+ and that oxygen vacancies are present. To visualize the distribution of Ce^{3+}, the oxygen vacancies, HAADF signals, and EELS spectra were simultaneously recorded while scanning the electron probe inside the red dotted box shown in Figure 2b. This technique is called "spectrum imaging".[28] The corresponding HAADF image and the M_5/M_4 ratio map are shown in Figure 2d. The colors in the M_5/M_4 ratio map indicate the valence state of Ce. Oxygen vacancies exist not only at the very surface region but also inside the nanoparticle with a thickness of ≈3.5 nm. The results obtained for an octahedral CeO_2 nanoparticle with an effective size of 100 nm are shown in Figure 2e–g. Interestingly, the region with oxygen vacancies is narrower for the octahedral CeO_2 nanoparticle with a thickness of ≈2.5 nm. This result is consistent with the previous reports that it is difficult to reduce (111) plane compared to (100) plane.[19,20]

Since individual nanoparticles can have different amounts of oxygen vacancies, EELS measurements were performed for several nanoparticles with different particle sizes to reveal the overall picture for the thickness of regions with oxygen vacancies (**Figure 3**). The solid circles and squares correspond to the results for the original samples. The open circles and squares are the results for the samples reduced at 400 °C, as will be discussed later. While the regions with oxygen vacancies are thin and have a narrow thickness distribution (2–4 nm) for o-CeO_2, they are thicker and have a wider thickness distribution (2–9 nm) for c-CeO_2. It is well known that smaller CeO_2 nanoparticles contain more oxygen vacancies at the surfaces.[24,26] Therefore, the difference in the thickness of regions with oxygen vacancies can be due to the size effect since c-CeO_2 is smaller than o-CeO_2. However, such an effect typically manifests itself in nanoparticles <15 nm in size and is not applicable to the present nanoparticles.

EELS measurements were also performed for several nanoparticles after H_2 reduction at 400 °C followed by quenching

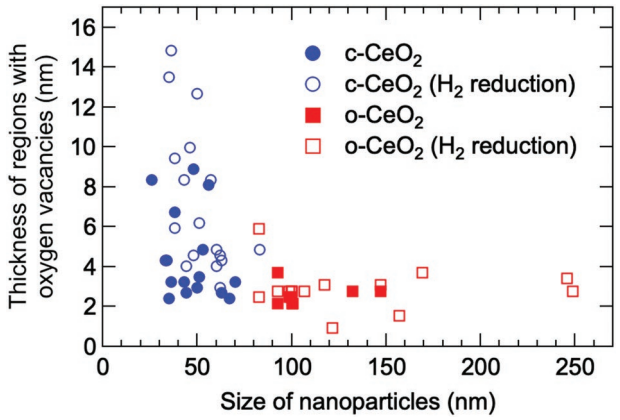

Figure 3. Particle-size-dependence of the thickness of regions with oxygen vacancies for c-CeO_2 and o-CeO_2. The solid circles and squares correspond to the results obtained for the original samples, and the open circles and squares are the results obtained for the samples reduced at 400 °C.

to room temperature to understand the lattice-plane-dependent reduction process. The results are shown as open circles and squares in Figure 3. The reduction temperature of 400 °C is above the position of the low-temperature peak in H_2-TPR for c-CeO_2 but below that for o-CeO_2 (Figure 1c). As expected, the thickness of regions with oxygen vacancies is increased as a whole only for c-CeO_2, although there is some variation in the thickness of regions with oxygen vacancies. It is interesting to note that the regions with oxygen vacancies extend to the interior regions, indicating that the reduction of the bulk oxygen instead of only the reduction of the surface oxygen makes no small contribution to the low-temperature peak.

To obtain direct evidence for the difference in activities of lattice oxygen in c-CeO_2 and o-CeO_2, we tracked the change in the amount of oxygen vacancies for identical nanoparticles before and after the ex situ reduction treatment using TEM grids that can endure high-temperature reduction treatments. **Figure 4**a,b compares the HAADF images and the M_5/M_4 ratio maps at identical regions before and after the reduction treatments at 400 °C for c-CeO_2 and o-CeO_2, respectively. It can be clearly observed that the thickness of regions with oxygen vacancies is drastically increased only for c-CeO_2. To reveal the dependence of oxygen vacancy formation on reduction temperature, H_2 reduction treatment was also performed at 600 °C for o-CeO_2, which is above the low-temperature peak in H_2-TPR. Contrary to our expectation, as shown in Figure S2 (Supporting Information), the thickness of regions with oxygen vacancies remains narrow, indicating that oxygen vacancies formed by the reduction treatment cannot be preserved for the case of the (111) planes.

Here, the reduction mechanism for CeO_2 is discussed. H_2-TPR measurements reveal that the reduction of both c-CeO_2 and o-CeO_2 proceeds via two steps, as previously reported. The first step is conventionally ascribed to the removal of "surface oxygen". However, as revealed by the systematic STEM-EELS measurements after reduction at 400 °C, the regions with oxygen vacancies extend to the interior regions for c-CeO_2, and there exist variations in the thickness of regions with oxygen vacancies from nanoparticle to nanoparticle. Therefore, the picture that the low-temperature peak is due to the reduction of the "surface oxygen" does not appropriately describe the reduction process of CeO_2, at least for c-CeO_2. Meanwhile, according to the phase diagram of CeO_{2-x}, it is well known

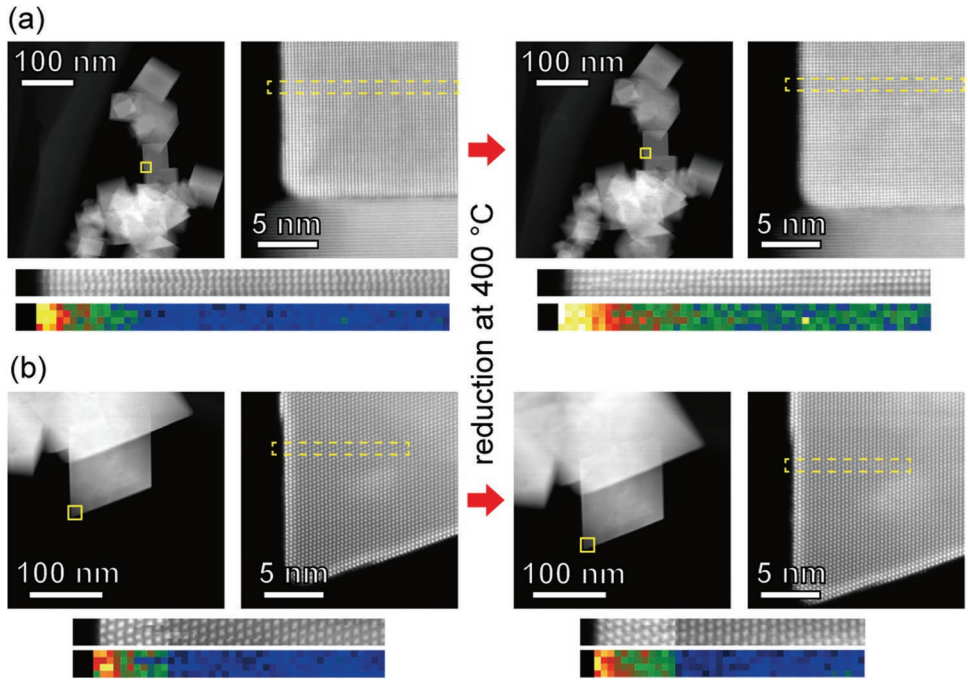

Figure 4. HAADF images and M_5/M_4 ratio maps at identical regions before and after the reduction treatments at 400 °C for a) c-CeO_2 and b) o-CeO_2. The yellow square in each left-side figure corresponds to the area, where the magnified HAADF image at the right side was obtained. Yellow-dotted rectangles show the regions where spectrum imaging was performed. The color legend for the M_5/M_4 ratio is the same as that shown in Figure 2.

that a miscibility gap exists between $Ce_{11}O_{20}$ ($CeO_{1.818}$) and CeO_2, and the maximum in the dome-shaped curve occurs at $2–x = 1.93$ and 637 °C.[29] Since the H_2-TPR measurements are typically performed in thermodynamically nonequilibrium conditions, direct comparison of the existing phases at certain temperatures is difficult, but the formation of the $CeO_{1.818}$ phase is most likely the origin of the low-temperature peak in the H_2-TPR profile. Above 637 °C, the miscibility gap disappears, and only the continuous reduction of CeO_2 proceeds, which contributes to the high-temperature peak observed in the H_2-TPR profile. Indeed, the valence state of Ce remains almost constant (green in the color legend) in the interior regions after reduction treatment at 400 °C, as shown in Figure 4. This corresponds to an M_5/M_4 ratio of ≈1.0 and an oxygen stoichiometry of ≈$CeO_{1.83}$, which is in fair agreement with $CeO_{1.818}$. When $CeO_{1.818}$ formation is the origin of the low-temperature peak in the H_2-TPR profiles, the different behavior of the (100) and (111) planes, including the positions of the low-temperature peaks, the amount of oxygen vacancies, and the stability of the oxygen vacancies, might be explained based on the structure of $CeO_{1.818}$. We have performed preliminary nano beam electron diffraction experiments for c-CeO_2 reduce at 400 °C along the [100] zone axis. The typical diffraction patterns obtained from the regions with the M_5/M_4 ratios of ≈0.9, 1.0, and 1.25 (mainly blue, green, and orange-to-yellow in the color legend, respectively) are shown in Figure S3 (Supporting Information). As expected, the diffraction patterns obtained from the blue region was typical of a fluorite structure (Figure S3a, Supporting Information). The diffraction pattern obtained from the green region was also the same as that of a fluorite structure (Figure S3b, Supporting Information). Note that this result does not necessarily mean that the crystal structure at the green region is not the $CeO_{1.818}$ phase because the $CeO_{1.818}$ phase basically gives the same diffraction pattern as an ideal fluorite structure along the pseudocubic [100] zone axis.[30] Systematic electron diffraction observations along different zone axes are necessary to identify the possible $CeO_{1.818}$ phase, but this is beyond the scope of this study. Interestingly, additional diffraction spots were observed at the orange-to-yellow region (Figure S3c, Supporting Information), which is consistent with the $CeO_{1.68}$ phase.[30] This result at least indicates that more than just the removal of the capping oxygen takes place at the surface of nanoparticles.

Finally, we will discuss the present results in light of previous reports on shape-controlled CeO_2. Our EELS observations revealed that the very surfaces (<≈2 nm) of both c-CeO_2 and o-CeO_2 contain considerable amounts of Ce^{3+}, but the distribution of Ce^{3+}, and, hence, the oxygen vacancies from the surface to the bulk regions, is different for c-CeO_2 and o-CeO_2 especially after the reduction treatment. The amounts of Ce^{3+} have been investigated for shape-controlled CeO_2 by several authors using X-ray photoelectron spectroscopy (XPS) with Al Kα (1.487 keV) or Mg Kα (1.253 keV) X-ray radiations. Zhou et al. reported that only Ce^{4+} could be detected for CeO_2 nanorods, which supposedly expose (100) and (110) planes, and CeO_2 nanoparticles, which supposedly expose (111) plane.[4] Likewise, Wu et al. found that the amount of Ce^{3+} was very small even if Ce^{3+} exists and similar for CeO_2 nanorods, nano-octahedra and nanocubes calcined at 400 °C.[19] Meanwhile, it was reported that the amounts of Ce^{3+} were ≈14%[13] and 17%[31] for both cubic and octahedral CeO_2. Note that the amount of Ce^{3+} was estimated for CeO_2 (111) model surfaces to be 2% assuming that Ce atoms on the terrace perimeter were of 3+ character.[32] Although the origin of discrepancy in the amount of Ce^{3+} among these reports is not clear, it is worth noting that the amounts of Ce^{3+} are similar for CeO_2 with different shapes, indicating that the XPS spectra are similar within each report. Since the inelastic mean free path (IMFP) of an electron in CeO_2 is 2.1 nm at 1.3 keV kinetic energy,[33] XPS spectra mainly include information from the surface region with the depth in the order of the IMFP length. Therefore, even if the reduced area extends to more interior regions, XPS measurements would not be able to detect information from the interior regions and would give essentially the same XPS spectra. Moreover, XPS measurements give average information of whole samples. In this regard, the advantage of EELS measurement is that we can study the depth profile of particular lattice planes of each nanoparticle when we observe them in edge-on conditions as long as the sample is thin enough along the electron propagation direction.

On the other hand, Wu et al. also systematically studied the UV Raman spectra, which is less surface sensitive technique compared to XPS, of CeO_2 nanorods, nano-octahedra, and nanocubes reduced at various temperatures from 400 to 600 °C. Assuming that a shoulder peak at ≈560 cm^{-1} was due to defect sites created by reduction, they reported that the amount of defect sites in the subsurface/bulk increased on average as the reduction temperature increased for nanorods and nanocubes while essentially no change in the spectra feature was observed for nano-octahedra. This is result is basically consistent with our observations. Still, EELS measurements have an advantage that we can study the distribution of oxygen vacancies of each nanoparticle.

3. Conclusion

In conclusion, we fabricated shape-controlled CeO_2 nanoparticles and systematically studied the catalytic activities of these nanoparticles and the distribution of surface oxygen vacancies on the (100) and (111) surfaces, including the response to H_2 reduction treatment. We successfully demonstrate that both catalytic activities and the ability to form oxygen vacancies are strongly dependent on the type of lattice planes, revealing direct evidence for a close relationship between the two. Moreover, we demonstrate that bulk oxygen instead of the widely believed surface capping oxygen makes no small contribution to the initial reduction step, which can be the origin of the low-temperature peak observed in the H_2-TPR profile. Our present study not only promotes the further fundamental study of CeO_2 catalysts but is also a significant step forward for realizing high-performance CeO_2-based catalysts.

4. Experimental Section

Synthesis of Cubic and Octahedral CeO_2 Nanoparticles: c-CeO_2 and o-CeO_2 were prepared using a hydrothermal method based on previous reports[34,35] that was optimized to yield highly crystalline and faceted nanocrystals. For the synthesis of c-CeO_2, an aqueous solution of $Ce(NO_3)_3{\cdot}6H_2O$ (5 mL and 0.13 M) was added dropwise into a NaOH solution (10 mL and 8.33 M) in a 23 mL Teflon bottle under vigorous stirring. Excess NO^{3-}, which is known to work as a capping agent, was introduced by adding 8.33 g of $NaNO_3$ to the solution. After additional

stirring for 30 min at room temperature, the Teflon bottle was sealed and hydrothermally treated in a stainless-steel autoclave at 180 °C for 24 h. For the synthesis of o-CeO_2, $Ce(NO_3)_3{\cdot}6H_2O$ (5 mL and 0.40 M) was added dropwise into Na_3PO_4 solution (10 mL and 0.0020 M) in a 23 mL Teflon bottle under vigorous stirring. After additional stirring for 30 min at room temperature, the Teflon bottle was sealed and hydrothermally treated in a stainless-steel autoclave at 200 °C for 24 h. Upon leaving the solution to cool to room temperature, the precipitates were separated by centrifugation, washed with distilled water and ethanol, and then dried at 60 °C for 12 h. Both samples were annealed at 450 °C in air to minimize possible variation in the crystallinity and/or amount of oxygen vacancies due to the difference in the synthesis conditions.

Characterization Techniques: The crystal structure of the samples was characterized by XRD (Rigaku, Ultima IV) with Cu-Ka radiation. The BET surface area was measured by nitrogen sorption at 77 K on a surface area analyzer (BELSORP-mini, MicrotracBEL Corp.). H_2-TPR was carried out in a flow of 5% H_2 and N_2 balance at a ramping rate of 5 °C min^{-1} using a BEL-CAT (BEL Japan). Catalytic CO oxidation was carried out with a fixed bed flow reactor. CeO_2 nanoparticles (20 mg) were loaded into a U-shaped glass tube, and the reaction gas (CO 0.5%, O_2 0.25%, He balance) was fed to the reactor at a flow rate of 500 mL min^{-1}. STEM observation was conducted using a Titan G2 Cubed (Thermo Fisher Scientific Inc.) operated at 300 kV. EELS spectra were acquired by using a Quantum spectrometer (Gatan Inc.) with monochromatic excitation to attain an energy resolution of 0.25 eV. For STEM observations, the probe-forming semiangle was set to 21.4 mrad. HAADF images were recorded with a detection angle range of 38 and 184 mrad. Probe currents of 50 pA were used for both STEM observations and EELS measurements. The spectrum images were typically acquired by scanning in 0.5 nm steps with an integration time of 0.5 s. Nano beam electron diffraction patterns were obtained also using Titan G2 cubed with the probe size of <≈3 nm and with the probe currents of 100 pA.

Supporting Information

Supporting Information is available from the Wiley Online Library or from the author.

Acknowledgements

This study was supported by the Japan Science and Technology Agency (JST) FOREST project (grant no. JPMJFR201UA), JSPS KAKENHI (grant no. 20H02824), and Asahi Glass Foundation.

Conflict of Interest

The authors declare no conflict of interest.

Data Availability Statement

The data that support the findings of this study are available from the corresponding author upon reasonable request.

Keywords

CeO_2, electron energy-loss spectroscopy, reduction mechanism, shape-controlled nanoparticles

Received: September 5, 2022
Revised: November 18, 2022
Published online: December 9, 2022

[1] A. Trovarelli, *Catal. Rev.: Sci. Eng.* **1996**, *38*, 439.
[2] T. Montini, M. Melchionna, M. Monai, P. Fornasiero, *Chem. Rev.* **2016**, *116*, 5987.
[3] F. Giordano, A. Trovarelli, C. de Leitenburg, M. Giona, *J. Catal.* **2000**, *193*, 273.
[4] K. B. Zhou, X. Wang, X. M. Sun, Q. Peng, Y. D. Li, *J. Catal.* **2005**, *229*, 206.
[5] M. L. Z. Tana, J. Li, H. J. Li, Y. Li, W. J. Shen, *Catal. Today* **2009**, *148*, 179.
[6] J. P. Holgado, R. Alvarez, G. Munuera, *Appl. Surf. Sci.* **2000**, *161*, 301.
[7] O. H. Laguna, M. A. Centeno, F. Romero-Sarria, J. A. Odriozola, *Catal. Today* **2011**, *172*, 118.
[8] H. C. Yao, Y. F. Y. Yao, *J. Catal.* **1984**, *86*, 254.
[9] C. W. Sun, H. Li, L. Q. Chen, *Environ. Sci.* **2012**, *5*, 8475.
[10] C. W. Sun, H. Li, L. Q. Chen, *J. Phys. Chem. Solids* **2007**, *68*, 1785.
[11] C. W. Sun, J. Sun, G. L. Xiao, H. R. Zhang, X. P. Qiu, H. Li, L. Q. Chen, *J. Phys. Chem. B* **2006**, *110*, 13445.
[12] Z. L. Wu, M. J. Li, S. H. Overbury, *J. Catal.* **2012**, *285*, 61.
[13] L. Torrente-Murciano, A. Gilbank, B. Puertolas, T. Garcia, B. Solsona, D. Chadwick, *Appl. Catal., B* **2013**, *132*, 116.
[14] M. Nolan, J. E. Fearon, G. W. Watson, *Solid State Ionics* **2006**, *177*, 3069.
[15] S. Fabris, G. Vicario, G. Balducci, S. de Gironcoli, S. Baroni, *J. Phys. Chem. B* **2005**, *109*, 22860.
[16] A. D. Mayernick, M. J. Janik, *J. Phys. Chem. C* **2008**, *112*, 14955.
[17] W. Q. Li, S. G. Srinivasan, D. R. Salahub, T. Heine, *Phys. Chem. Chem. Phys.* **2016**, *18*, 11139.
[18] W. Zhang, M. Pu, M. Lei, *Langmuir* **2020**, *36*, 5891.
[19] Z. L. Wu, M. J. Li, J. Howe, H. M. Meyer, S. H. Overbury, *Langmuir* **2010**, *26*, 16595.
[20] T. Desaunay, G. Bonura, V. Chiodo, S. Freni, J. P. Couzinie, J. Bourgon, A. Ringuede, F. Labat, C. Adamo, M. Cassir, *J. Catal.* **2013**, *297*, 193.
[21] H. Hojo, T. Mizoguchi, H. Ohta, S. D. Findlay, N. Shibata, T. Yamamoto, Y. Ikuhara, *Nano Lett.* **2010**, *10*, 4668.
[22] B. Feng, H. Hojo, T. Mizoguchi, H. Ohta, S. D. Findlay, Y. Sato, N. Shibata, T. Yamamoto, Y. Ikuhara, *Appl. Phys. Lett.* **2012**, *100*, 073109.
[23] B. Feng, I. Sugiyama, H. Hojo, H. Ohta, N. Shibata, Y. Ikuhara, *Sci. Rep.* **2016**, *6*, 20288.
[24] L. J. Wu, H. J. Wiesmann, A. R. Moodenbaugh, R. F. Klie, Y. M. Zhu, D. O. Welch, M. Suenaga, *Phys. Rev. B* **2004**, *69*, 125415.
[25] S. Turner, S. Lazar, B. Freitag, R. Egoavil, J. Verbeeck, S. Put, Y. Strauven, G. Van Tendeloo, *Nanoscale* **2011**, *3*, 3385.
[26] X. D. Hao, A. Yoko, C. L. Chen, K. Inoue, M. Saito, G. Seong, S. Takami, T. Adschiri, Y. Ikuhara, *Small* **2018**, *14*, 1802915.
[27] B. Goris, S. Turner, S. Bals, G. Van Tendeloo, *ACS Nano* **2014**, *8*, 10878.
[28] J. A. Hunt, D. B. Williams, *Ultramicroscopy* **1991**, *38*, 47.
[29] M. Ricken, J. Nolting, I. Riess, *J. Solid State Chem.* **1984**, *54*, 89.
[30] E. A. Kummerle, G. Heger, *J. Solid State Chem.* **1999**, *147*, 485.
[31] G. Seong, M. Dejhosseini, T. Adschiri, *Appl. Catal., A* **2018**, *550*, 284.
[32] J. L. Lu, H. J. Gao, S. Shaikhutdinov, H. J. Freund, *Surf. Sci.* **2006**, *600*, 5004.
[33] S. Kato, M. Ammann, T. Huthwelker, C. Paun, M. Lampimaki, M. T. Lee, M. Rothensteiner, J. A. van Bokhoven, *Phys. Chem. Chem. Phys.* **2015**, *17*, 5078.
[34] Q. Wu, F. Zhang, P. Xiao, H. S. Tao, X. Z. Wang, Z. Hu, Y. N. Lu, *J. Phys. Chem. C* **2008**, *112*, 17076.
[35] L. Yan, R. B. Yu, J. Chen, X. R. Xing, *Cryst. Growth Des.* **2008**, *8*, 1474.